

# Jamming the Random Lorentz Gas: Configurational Entropy, Crunching Geometry, and Critical Universality

Giampaolo Folena,<sup>1</sup> Patrick Charbonneau,<sup>2,3</sup> Peter K. Morse,<sup>4</sup>  
Rafael Díaz Hernández Rojas,<sup>5</sup> and Federico Ricci-Tersenghi<sup>6</sup>

<sup>1</sup>*Independent Researcher\**

<sup>2</sup>*Department of Chemistry, Duke University, Durham, North Carolina 27708*

<sup>3</sup>*Department of Physics, Duke University, Durham, North Carolina 27708*

<sup>4</sup>*Department of Physics, Seton Hall University, South Orange, NJ 07079*

<sup>5</sup>*Institute for Theoretical Physics, Georg-August-Universität Göttingen, Göttingen, Germany*

<sup>6</sup>*Dipartimento di Fisica, Sapienza Università di Roma, INFN – Sezione di Roma1,  
and CNR – Nanotec, Piazzale Aldo Moro 5, Roma 00185 Italy*

**Abstract:** Deterministic optimization algorithms unequivocally partition a complex energy landscape in inherent structures (ISs) and their respective basins of attraction. But can these basins be defined solely through geometric principles? This question is particularly important when examining the jamming of hard spheres. We here consider this issue by proposing a geometric class of gradient descent-like algorithms, which we use to study a system in the hard-sphere universality class, the random Lorentz gas. The statistics of the resulting IS is found to be strictly inherited from those of Poisson–Voronoi tessellations. The landscape roughness is further found to give rise to a hierarchical organization of ISs which various algorithms explore differently. In particular, greedy and reluctant schemes tend to favor ISs of markedly different densities. The resulting ISs nevertheless robustly exhibit a universal force distribution, thus confirming the geometric nature of the jamming universality class.

*Introduction* – Jamming granular systems – either for sand play or industrial transport [1] – ubiquitously gives rise to disordered materials; so does supercooling many liquids. Over a quarter of a century ago, this analogy led Liu and Nagel to propose a unification of the two processes under a single conceptual umbrella [2]. Their *jamming phase diagram* has since inspired fields as diverse as robotics [3], tissue mechanics [4], and neural networks [5, 6]. It has also seeded a substantial research effort aiming to flesh out the original proposal itself [7–9].

In this last respect, particularly significant strides have been made from the study of simple liquids in the limit of infinite spatial dimensions,  $d \rightarrow \infty$  [10, 11]. This seemingly abstract construction has indeed rationalized jamming marginality [12, 13] and its associated isostaticity [14–16], and made stunningly accurate predictions about the non-trivial scaling of the distribution of weak interparticle forces  $P_F(f) \sim f^\theta$  and small interparticle gaps  $P_H(h) \sim h^\gamma$  down to  $d = 2$  [15, 17–23]. Despite jamming being an inherently out-of-equilibrium phenomenon, and hence a protocol dependent process, its criticality is seemingly universal. That robustness, however, remains largely unexplained.

Another – in some ways more salient – theoretical challenge entails predicting the jamming density. For three-dimensional hard spheres, that quantity had long been understood to be algorithm invariant, with a volume fraction of about 64%, thus cementing *random close packing* as a physically robust and universal concept. Over the last couple of decades, however, the confounding role played by various factors, such as the degree of crystallinity [24] and the preparation

scheme [19, 21, 25], including the choice of initial conditions [21, 26], have softened that apparent robustness. At this point, even identifying a physically (let alone mathematically [27, p. 240–2]) meaningful observable remains an open challenge.

Some of us have recently proposed that a well-defined quantity might be “the lowest jammed density achievable through bulk physical processes involving monotonic compression”,  $\varphi_{J0}$  [25]. Put differently, one would like to identify an algorithm for jamming hard spheres akin to gradient descent (GD) for energy minimization in that it is greedy and local. This idea is not new. In the mid-1980s, Stillinger and Weber systematically approximated the jammed inherent structures (IS) of hard spheres by using GD for systems with ever steeper interactions [28]. More recently, Torquato and Jiao have formulated a linear programming scheme for hard spheres to reach jamming [29] – later generalized as CALiPPSO [30] – and Lerner et al. have formulated an overdamped compression scheme for that same purpose [15]. For various reasons, however, the effectiveness of these schemes at attaining  $\varphi_{J0}$  has not been systematically evaluated. (See Ref. [25] for an effort along this direction.) More problematically, a qualitative understanding of the similarities and differences between these schemes has yet to be teased out. Even in the simplifying limit  $d \rightarrow \infty$  (out-of-equilibrium) insights are in short supply [31].

In order to shed a new light on both jamming robustness and density, we here consider the random Lorentz gas (RLG), a single-particle model that belongs to the hard sphere universality class in the limit  $d \rightarrow \infty$ . But what is jamming – an ostensibly collective phenomenon

– in a single-particle system? Inspired by a recent geometrical study [32], we propose a class of GD-like volume ascent (VA) algorithms for identifying jammed IS for this model. This approach determines  $\varphi_{J0}$  for the RLG and illuminates the algorithm dependence of jamming more generally. Remarkably, we also find that  $P_F(f)$  converges to the anomalous infinite-dimensional hard-sphere scaling for all algorithms, thus illuminating its geometrical origin. These advances not only pave the way for a deeper understanding of jamming but also hold the potential for improving high-dimensional optimization with hard constraints, which notably appear in computational geometry [33–35] and robust optimization [36].

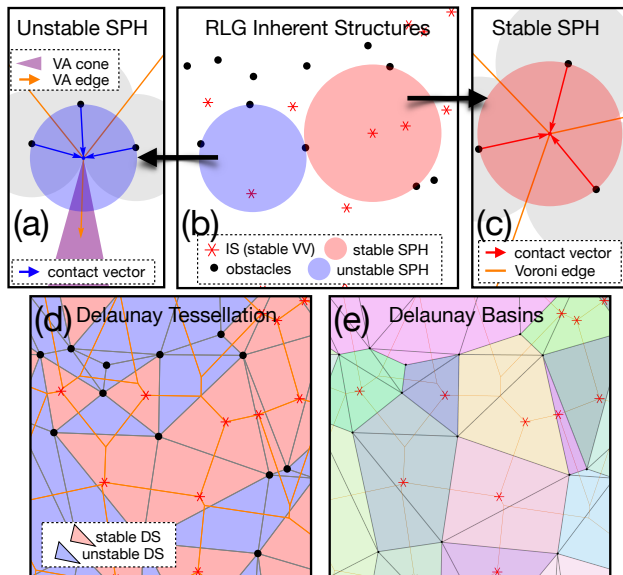


FIG. 1. **(b)**: Geometric (or entropic) landscape of the  $d = 2$  RLG with obstacles (black dots) and IS (red stars). A SPH has  $d + 1$  obstacles in contact; it is unstable if these contacts are co-hemispheric (light blue) and stable otherwise (light red). Contact vectors for the unstable **(a)** and stable **(c)** SPH in **(b)**, along with the VA cone of possible expansion directions (purple) for the former. **(d)**: Delaunay tessellation of the sample in **(b)**. An unstable DS does not contain its circumcenter (blue), while a stable DS does (red), thus identifying an IS (stars). **(e)**: Delaunay basins (differently colored; Eq. 4) of the sample in **(b)**. These basins are generally composed of one stable DS and zero or more surrounding unstable DS. DS (black lines) and the Voronoi tessellation (orange lines) are provided as reference.

*The Entropic Landscape of the RLG* – Recall that the RLG consists of one spherical tracer evolving in the space unoccupied by hard (yet non-interacting) fixed spherical obstacles. These obstacles, which are distributed uniformly at random form a Poisson process with number density (or intensity)  $\rho = N/V$ . One RLG convention assigns both tracer and obstacles the same sphere radius  $r/2$ ; equivalently, one could consider a point tracer and obstacles with radius  $r$  or point ob-

stacles and a tracer with radius  $r$ . To ease visualization, we here mainly follow this last convention. To make densities unitless and of order one in all  $d$ , we further set  $\rho = 1$  and define the reduced volume fraction  $\hat{\varphi} = \rho V_d r^d / d = V_d r^d / d$  with  $V_d$  the volume of a  $d$ -dimensional unit sphere.

In order to study jamming in the RLG, we first identify its IS, following the approach developed for random polytopes in Ref. [32]. At equilibrium,  $r$  is constant; compression inflates  $r$ . At each tracer position  $\mathbf{x}$  there exists a maximal sphere (SPH) of radius  $r_{\text{SPH}}$ , that does not overlap with any obstacles. IS are obtained when that radius  $r_{\text{SPH}}$  can no longer locally grow by changing position  $\mathbf{x}$ , without creating overlaps with obstacles, hence determining  $r_{\text{IS}}$ . The resulting tracer position,  $\mathbf{x}_{\text{IS}}$ , is then equidistant from  $d + 1$  obstacles: fewer would not ensure mechanical stability, and more would be highly improbable. Per the Maxwell criterion, the resulting IS is therefore isostatic. Given this analysis, an unambiguous determination of all IS for a given obstacle distribution is possible (see Fig. 1b). In geometrical terms, each point equidistant to  $d + 1$  obstacles is a Voronoi vertex (VV) or, equivalently, a circumcenter of the dual Delaunay tessellation. As shown in Ref. [37], a VV is *stable* if it is contained within the respective Delaunay simplex (DS), and *unstable* if not. Only the former are IS (see Fig. 1a-d).

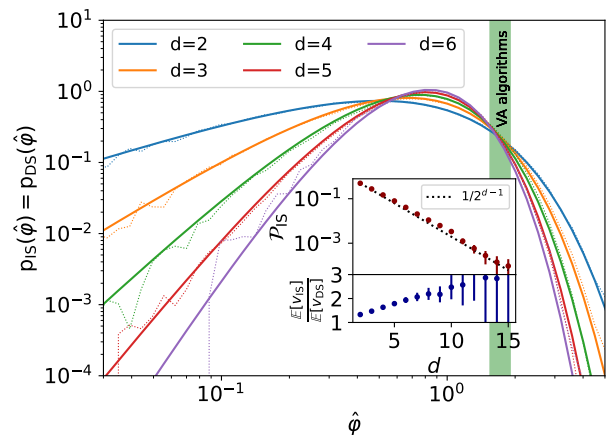


FIG. 2. Probability distribution of the packing fraction  $\hat{\varphi}_{\text{IS}}$  for IS in  $d = 2 \dots 6$ . The analytical expression from Eq. (2) (full lines) fully agrees with numerical results obtained by enumerating stable DS (dotted lines). Note that the distribution peaks at  $(d - 1)/d$ , with the left tail scaling as  $x^{d-1}$  and the right tail as  $e^{-dx}$ . For all  $d$ , the expected jamming packing fraction,  $\mathbb{E}[\hat{\varphi}_{\text{IS}}] = 1$ , but VA algorithms typically reach larger values, as can be seen for  $d = 2 \dots 6$  (green band). (inset) The proportion of stable DS (points) empirically scales as  $1/2^{d-1}$  (dotted line), while the ratio between the typical volume of stable DS and the typical volume of all DS grows sublinearly in  $d$ .

*Number of IS* – Having established that each IS is the circumcenter of a stable DS, we now proceed to count these features as a function of their packing fraction at jamming,  $\hat{\varphi}_{\text{IS}}$  (or, equivalently,  $r_{\text{IS}}$ ), thus providing a measure of configurational entropy.

Results from stochastic geometry give that the density of all (stable and unstable) DS per unit volume with given  $\hat{\varphi}$  is

$$\mathcal{N}_{\text{DS}}(\hat{\varphi}) = N_{\text{DS}}(d)p_{\text{DS}}(\hat{\varphi}), \quad p_{\text{DS}}(\hat{\varphi}) = \frac{d^d e^{-d\hat{\varphi}} \hat{\varphi}^{d-1}}{\Gamma(d)} \quad (1)$$

where  $N_{\text{DS}}(d)$  is the total number of DS per unit volume and  $p_{\text{DS}}(\hat{\varphi})$  is their probability distribution function (pdf), with expectation  $\mathbb{E}_{\text{DS}}[\hat{\varphi}] = 1$  for all  $d$  [38, 39]. Remarkably, given [40, Thm. (10.4.4)], the geometry of each DS is statistically independent of its radial size [41] – or, equivalently the DS radial size distribution is invariant when conditioned on stable D – and hence the pdf of IS and DS are the same,

$$p_{\text{IS}}(\hat{\varphi}) = p_{\text{DS}}(\hat{\varphi}). \quad (2)$$

The number of IS per unit volume  $N_{\text{IS}}(d) = \mathcal{V}_{\text{IS}}(d)\mathcal{N}_{\text{DS}}(d)$ , however, is strongly reduced. The proportionality factor can be decomposed in  $\mathcal{V}_{\text{IS}}(d) = \mathcal{P}_{\text{IS}}(d)\mathbb{E}[v_{\text{IS}}]/\mathbb{E}[v_{\text{DS}}]$ , where  $\mathcal{P}_{\text{IS}}(d)$  is the fraction of stable DS and  $\mathbb{E}[v_{\text{IS}}]/\mathbb{E}[v_{\text{DS}}]$  is the ratio of the expected volume of stable DS to the expected volume of generic DS.

Figure 2 shows that the normalized IS pdf (expectedly) agrees with numerical results. Numerical simulations (see Fig. 2 inset) further reveal that the proportion of stable DS  $\mathcal{P}_{\text{IS}}(d)$  is exponentially suppressed in  $d$ , approximately scaling as  $1/2^{d-1}$  [42], while the ratio of volumes  $\mathbb{E}[v_{\text{IS}}]/\mathbb{E}[v_{\text{DS}}]$  grows slower than linearly with  $d$ . In other words, in high  $d$  unstable DS dominate while IS are rare. Moreover, in all  $d$  sampling IS uniformly at random gives  $\mathbb{E}_{\text{IS}}[\hat{\varphi}] = 1$ .

*VA algorithm and geometry* – Despite the scarcity of stable DS, some algorithms can nevertheless attain them in polynomial time. To this effect, we here specifically define volume ascent (VA) schemes as the class of *local* algorithms which monotonically inflate  $r_{\text{SPH}}$ .

Note that the VA problem can also be formulated more generally within the mathematical framework of non-smooth optimization [43, 44]. Specifically,  $r_{\text{SPH}}$  is a continuous but non-differentiable function of  $\mathbf{x}$ , defining a rough landscape with many kinks, which cannot be optimized by standard optimization techniques. We here proceed with a specific analysis of stable DS, which provides insight into the dynamics of these algorithms.

First, each unstable DS is associated with a VV that presents a cone of possible VA directions (VA cone), within which the edges of the Voronoi tessellation identify a subset of specific VA pathways (VA edges). While in  $d = 2$  an unstable VV contains only one such VA edge

(see Fig. 1a), for  $d > 2$  the number of VA edges for an unstable VV varies between 1 and  $d - 1$ .

Second, recall that the fraction of stable DS scales as  $\mathcal{P}_{\text{IS}}(d) \sim 1/2^{d-1}$  and hence for large  $d$  the system volume is almost completely filled with unstable DS. Any VA algorithm must therefore flow between many unstable VVs before reaching an IS. Because VVs can be hierarchically connected through VA edges, selecting a specific VA algorithm is equivalent to selecting one such compression pathway (either along VA edges or in between them).

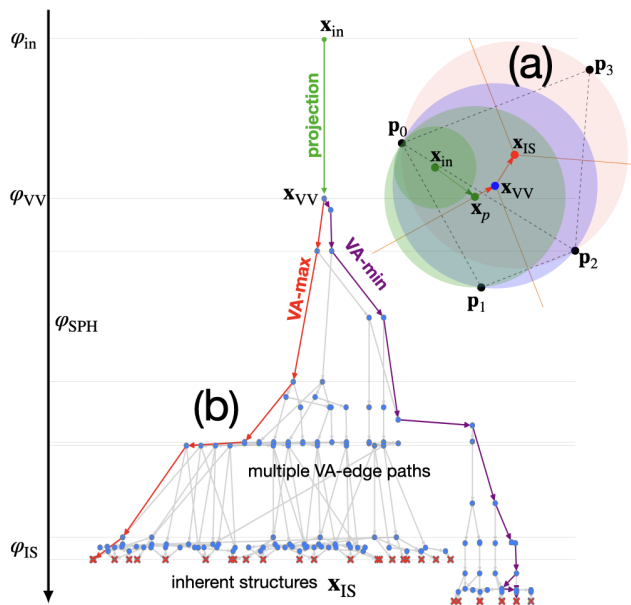


FIG. 3. **(a)**: Schematic of the VA-max algorithm for the  $d = 2$  RLG. The tracer starts at  $\mathbf{x}_{\text{in}}$ , moves radially from  $\mathbf{p}_0$  until it reaches the Voronoi line at  $\mathbf{x}_p$ , and then follows it until reaching the first VV at  $\mathbf{x}_{\text{VV}}$ . It subsequently follows the VA edge until  $\mathbf{x}_{\text{IS}}$ , which corresponds to a vertex of the Voronoi tessellation. **(b)**: In generic  $d$  dimension the VA cone at each VV can present up to  $d-1$  VA edges, thus leading to a multi-path structure of the VA-edge algorithm. For this  $d = 5$  example, the abscissa is arbitrarily chosen so as to minimize the number of crossings between paths. After the initial  $d$ -step projection up to  $\hat{\varphi}_{\text{VV}}$  (green), multi-furcation along various VA edges results in different IS (red crosses). Path coalescence can also arise, but is rare. The VA-max (red) and the VA-min (purple) paths are the greediest and the most reluctant VA-edge algorithms, respectively.

Among all possible VA algorithms, we first consider the *greediest* option, VA-max. The tracer displacement,  $d\mathbf{x}$ , is chosen to maximize the growth of the SPH radius,  $r_{\text{SPH}}$ , at each position  $\mathbf{x}$

$$d\mathbf{x} = \underset{d\tilde{\mathbf{x}}}{\operatorname{argmax}} r_{\text{SPH}}(\mathbf{x} + d\tilde{\mathbf{x}}), \quad (3)$$

making it a direct analog of GD for energy minimization. For a broader definition of steepest descent in non-smooth landscapes, refer to [44]. Figure 3(a) il-

illustrates the process for  $d = 2$ . Starting from a point tracer originally at  $\mathbf{x} = \mathbf{x}_{\text{in}} = \vec{0}$ , the maximal radius available  $r_{\text{SPH}}$  is equal to the distance to the closest obstacle  $|\mathbf{p}_0|$ . To maximize Eq. (3) the tracer then moves radially from the closest obstacle ( $d\mathbf{x} \propto -\mathbf{p}_0$ ) while its radius grows as  $r_{\text{SPH}} = |\mathbf{x} - \mathbf{p}_0|$ , until the tracer kisses a second obstacle at  $\mathbf{p}_1$ . Its center is then equidistant from  $\mathbf{p}_0$  and  $\mathbf{p}_1$ . In order to maximize Eq. (3) the subsequent dynamics follows the Voronoi hyperplane defined by points equidistant from both  $\mathbf{p}_0$  and  $\mathbf{p}_1$ , until the SPH reaches a third obstacle at  $\mathbf{p}_2$ . In  $d = 2$ , the tracer is then equidistant from  $d + 1 = 3$  obstacles, and its center is on a VV, by definition. In general  $d$ , following Eq. (3), the center of the SPH reaches a VV by  $d$  Gram-Schmidt projections of the initial growth direction  $-\mathbf{p}_0$  onto  $\text{span}\{\mathbf{p}_1, \dots, \mathbf{p}_d\}$ , thus defining  $\hat{\phi}_{\text{VV}}$ [45].

If this VV is stable, then an IS has been reached and the dynamics stops. Otherwise, the trajectory flows in the greediest direction inside the VA cone, which necessarily lies along one of the VA edges (see Fig. 1(a)). For  $d = 2$ , because the VA cone contains only one such edge, VA-max follows it up the next VV. In  $d > 2$  at each VV the greediest VA edge is followed until another VV is found, and so on. (Algorithmic details are reported in Appendix A.) Figure 3(b) illustrates the VA-max algorithm among the graph of VA edges connecting VVs. All other paths are *reluctant* versions. Among those, we also define the most reluctant VA-edge algorithm, VA-min, which selects the direction of least growth at each VV. (Note that this scheme is not the most reluctant algorithm of the overall VA class, for which an inf does not exist.) As expected [46], more reluctant algorithms typically achieve larger packing fractions  $\hat{\phi}_{\text{IS}}$ , over a larger number of steps than VA-max (see Appendix B). The graph of all possible VA-edge paths from the initial projection  $\mathbf{x}_{\text{VV}}$  to all final ISs presents two key features of rough landscapes: *multifurcation* and *coalescence*. The former is directly connected to the presence of multiple VA edges at each VV and its probability grows with  $d$ ; the latter is the convergence of two trajectories that have previously bifurcated and its probability vanishes as  $d$  increases.

*Fractal Basins* – The basin of attractions for a given (deterministic) algorithm is the ensemble of all initial configurations  $\mathbf{x}_{\text{in}}$  that reach a same IS. For VA-max in  $d = 2$ , a geometrical analysis of these basins is straightforward. Because every trajectory starting within a given DS flows towards the VV at its circumcenter, the flow of trajectories clusters all DSs that flow to the same IS. The basin of attraction of each IS is therefore a pure *Delaunay basin*

$$\mathcal{D}_{\text{IS}} = \{a \mid \text{circ}(a) = \mathbf{x}_{\text{IS}} \text{ or } \exists b \in \mathcal{D}_{\text{IS}} \text{ s.t. } \text{circ}(a) \subset b\}, \quad (4)$$

where  $a, b$  are DS and  $\text{circ}(a)$  is the circumcenter of  $a$ . Put differently, the basins of attraction can be decomposed as one stable DS surrounded by unstable DSs.

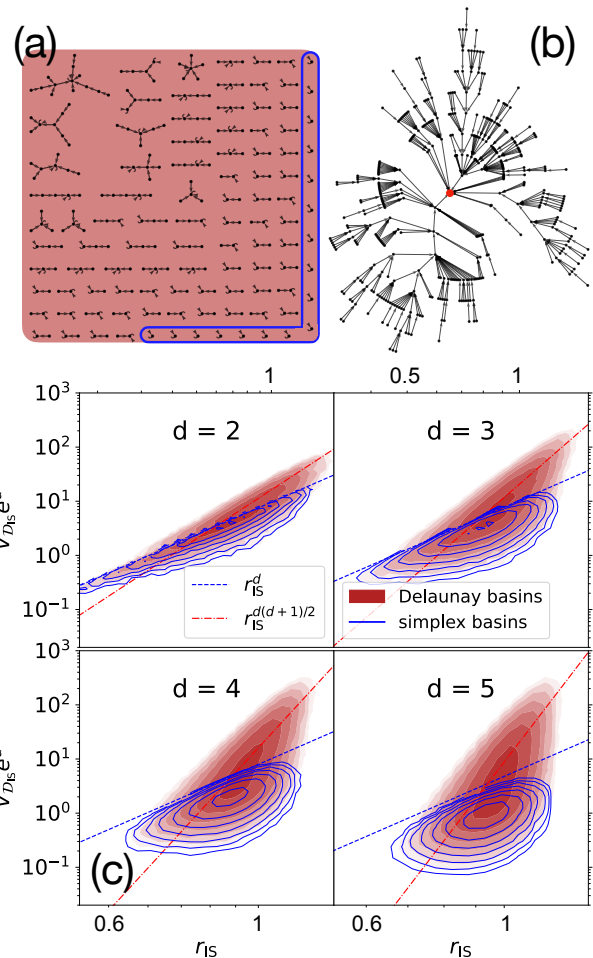


FIG. 4. (a): Tree graphs of Delaunay basins in  $d = 2$  (see Fig. 1e). The fraction of Delaunay basins consisting of a single DS (within blue line) relative to that of multi-DS basins decreases exponentially with increasing  $d$ . (b): Sample tree graph for a large Delaunay basin in  $d = 4$  illustrating the growing fractal structure of large basins with  $d$ . Edges denote the flow between unstable DS (black dots) up to the IS (red dot). (c): Joint distribution of the Delaunay basin volume  $V_{\mathcal{D}_{\text{IS}}}$  and circumradius  $r_{\text{IS}}$  in  $d = 2 \dots 5$ . The volume of basins composed of one simplex is upper bounded by the volume of regular simplexes (blue dashed line). The non-compact dependence of the volume of Delaunay basins (red cloud) trends as  $\propto r_{\text{IS}}^{d(d+1)/2}$  (red dashed-dotted line), hinting at their fractal nature. Both blue and red clouds are pdf on logarithmic scales with contour lines at  $2^k$  with  $k = -5 \dots 1$ .

Interestingly, Delaunay basins are exactly the basins of attraction of the CALiPPSO linear optimization algorithm [30] (see Appendix C for details). As can be seen in Fig. 1e, the resulting basins are heterogeneous in shape and not necessarily convex. For VA-max in  $d > 2$ , although a similar decomposition does not exactly describe basins – some of the initial simplexes having more than one unstable direction – numerical results suggest it is nevertheless a very good approximation, especially

for large  $d$ .

The characteristic tree-like organization of DS within a Delaunay basin (see Fig. 4b) hints at a fractal-like shape for polytopic basins. In order to characterize their organization more systematically, we consider the joint distribution of basin volume  $V_{\mathcal{D}_{\text{IS}}}$  and circumcenter radius  $r_{\text{IS}}$  (Fig. 4(c)). In all  $d$ , the basin volume grows much faster than for compact objects, for which  $V \propto r^d$ , consistent with basins becoming increasingly fractal-like with  $d$ . Given that the number of simplexes within a typical basin scales exponentially with  $d$  (due to the scarcity of stable DS), we therefore expect that even in moderately high dimensions, typical basins exhibit a distinctly fractal-like geometry.

The basin volume distribution further provides immediate insight into algorithmic outcomes. The basin volume of an algorithm reweighs the contribution of an IS relative to the uniform distribution (as in Fig. 2). For example Delaunay basins and the corresponding CALiPPSO algorithm are related by

$$\langle \varphi_{\text{IS}} \rangle_{\text{CAL}} = \sum_{\text{IS}} \frac{V_{\mathcal{D}_{\text{IS}}}}{V_{\text{tot}}} \varphi_{\text{IS}}. \quad (5)$$

Because IS with smaller  $\hat{\varphi}_{\text{IS}}$  tend to have much smaller  $V_{\mathcal{D}_{\text{IS}}}$  (and therefore less weight) than those with larger  $\hat{\varphi}_{\text{IS}}$ , the uniform measure,  $\mathbb{E}_{\text{IS}}[\hat{\varphi}] = 1$ , provides a lower bound to the jamming density achieved by VA algorithms. In addition, because for a fixed  $r_{\text{IS}}$  the basin volume distribution is wide, the Edwards hypothesis, which states that configurations with a given  $\hat{\varphi}_{\text{IS}}$  are sampled uniformly [47, 48], is also violated for all  $d$ .

*Jamming Results*– As generally expected for systems with a complex landscape [49–51], different optimization algorithms reach IS at different “depths”. Although the maximal radius  $r_{\text{IS}}$  achieved when starting within the basin of attraction of a particular IS is geometrically fixed, the probability of ending in that basin is algorithm dependent, as in Eq. (5). We here consider the performance of three different VA algorithms – (i) VA-max, (ii) VA-min, and (iii) force-min – as well as a non-local yet VA-like scheme, (iv) CALiPPSO. Recall that VA-max is by construction the *greediest* local algorithm for entropic landscapes, equivalent to the gradient descent scheme for energy landscapes, while VA-min is the *most reluctant* of all VA-edge algorithms. We also have that force-min [52, 53] is a VA reluctant algorithm that does not follow VV edges, and CALiPPSO is a non-local greedy scheme (see Appendix C and D for details). For these algorithms, Fig. 5(a) compares  $\langle \hat{\varphi}_{\text{IS}} \rangle_{\text{alg}}$ , averaging over both trajectories and realizations of disorder and starting from an initial density  $\hat{\varphi}_{\text{in}} = 0$ . In all cases, the results are markedly larger than the uniform sampling bound,  $\mathbb{E}[\hat{\varphi}_{\text{IS}}] = 1$ . As expected, VA-max gives the lowest jamming densities  $\hat{\varphi}_{\text{J0}} = \langle \hat{\varphi}_{\text{IS}} \rangle_{\text{VA-max}}$  in all  $d$  and CALiPPSO gives nearly indistinguishable results. In other words, VA-max reaches some of the least “sta-

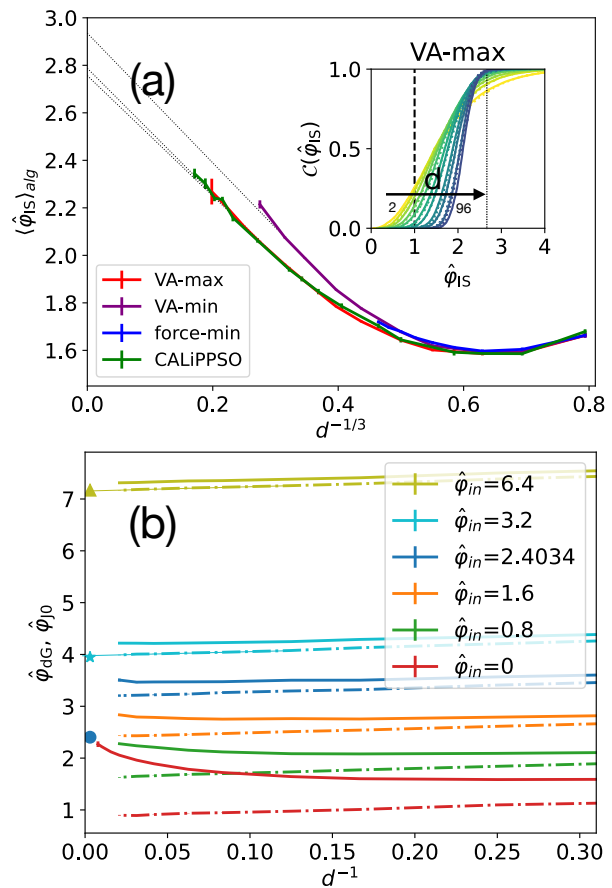


FIG. 5. **(a)**: Dimensional dependence of the average jamming density reached from  $\hat{\varphi}_{\text{in}} = 0$ ,  $\langle \hat{\varphi}_{\text{IS}} \rangle_{\text{alg}}$ , for four different algorithms: VA-max, VA-min, CALiPPSO and force-min. The empirical scaling  $d^{-1/3}$  ensures a (nearly) linear scaling at large  $d$ . Both VA-max, the greediest local algorithm, and CALiPPSO, its non-local equivalent, reach the same compression. Their extrapolation (thin dotted lines) suggests that  $\hat{\varphi}_{\text{J0}} = \langle \hat{\varphi}_{\text{IS}} \rangle_{\text{VA-max}} = 2.73(2)$  in the limit  $d \rightarrow \infty$ . In all  $d > 2$ , VA-min and force-min results are significantly larger with  $\langle \hat{\varphi}_{\text{IS}} \rangle_{\text{VA-min}} = 2.94(9)$  asymptotically **inset**: Cumulative distribution of  $\hat{\varphi}_{\text{IS}}$  for VA-max in  $d = 2 \dots 96$ . (CALiPPSO results are indistinguishable on this scale.) The expected value for a flat measure over ISs (dashed line) and  $\hat{\varphi}_{\text{J0}}$  in the limit  $d \rightarrow \infty$  (dotted line) are given as reference. **(b)**: Dimensional dependence of the jamming density  $\hat{\varphi}_{\text{J0}}$  (full lines) and the dynamical Gardner density  $\hat{\varphi}_{\text{dG}}$  (dashed-dotted lines) reached by VA-max from  $\hat{\varphi}_{\text{in}} = 0, 0.8, 1.6, 2.4034, 3.2, 6.4$ . (The red curve is the same as in (a).) The adiabatic Gardner transition for  $d \rightarrow \infty$  (symbols) are provided as reference for  $\hat{\varphi}_{\text{in}} \geq \hat{\varphi}_{\text{d}}$ . For  $\hat{\varphi}_{\text{in}} \gg \hat{\varphi}_{\text{d}}$ ,  $\hat{\varphi}_{\text{dG}}$  agrees well with  $\hat{\varphi}_{\text{G}}$  (see linear extrapolations in  $1/d$  for  $\hat{\varphi}_{\text{in}} = 3.2, 6.4$ ).

ble” IS. At the other end of the spectrum, VA-min and force-min give nearly identical results. Interestingly, the gap between the two pairs of algorithms enlarges with dimension, a reflection of the growing landscape complexity.

In order to relate these finite- $d$  findings with (puta-

tive) DMFT solutions for the limit  $d \rightarrow \infty$ , a dimensional extrapolation is needed. A simple  $1/d$  scaling, however, does not capture the trend of even the highest  $d$  results achieved, in marked contrast from what is observed for equilibrium observables in that same model [54, 55]. Recent results for other systems with complex landscapes suggest that altogether different finite-size scaling forms,  $d^{-a}$  with  $a < 1$ , are to be expected [50, 56], but limited theoretical guidance is available on choosing  $a$ . Unfortunately, that choice substantially impacts the extrapolation outcome, with the systematic error far exceeding the statistical one. For instance,  $a = 1/2$  gives  $\hat{\varphi}_{J0} = 2.49(2)$  at one end and  $a = 1/4$  gives  $\hat{\varphi}_{J0} = 3.09(2)$  at the other (fits are for  $d > 30$ ). This density range is nevertheless largely consistent with earlier estimates obtained by GD on a softened RLG [31] and by force-min on the many-body problem [57] (after appropriate rescaling [31]), especially given that these estimates were obtained from narrower  $d$  ranges and extrapolated with  $a = 1$ .

*Gardner transition* – Trajectories can also be started from finite initial (equilibrium) densities, i.e.,  $\hat{\varphi}_{\text{in}} > 0$ . Algorithms are then expected to reach IS that lie deeper in the landscape, as can be seen for VA-max in Fig. 5(b). Recall that in the limit  $d \rightarrow \infty$ , for  $\hat{\varphi}_{\text{in}} < \hat{\varphi}_d = 2.4034\dots$  the equilibrium dynamics of the RLG is ergodic, while for  $\hat{\varphi}_{\text{in}} > \hat{\varphi}_d$  it is localized to a cage. In the latter regime, a slow (adiabatic) compression as tracer remains inside its cage makes *state following* calculations possible. For each  $\hat{\varphi}_{\text{in}}$ , there then also exists a Gardner volume fraction  $\hat{\varphi}_G(\hat{\varphi}_{\text{in}})$  at which the cage structure fractures into a full hierarchy of subcages, a full replica symmetry breaking (fullRSB) transition[11]. From simulations, it has also been suggested that a Gardner-like transition might be generally observable in a fast (non-adiabatic) compression, but theoretical guidance is lacking [21].

The simplicity of the RLG landscape geometry makes a broader consideration of Gardner physics possible. Recall that the initial VA-max projection collapses trajectories onto a VV. In other words, a whole compact volume is reduced to a point. After this projection, the system explores the intricacies of the Voronoi edges that underlie landscape roughness (see Fig. 4). The end of the projection phase at volume fraction  $\hat{\varphi}_{\text{VV}}$  therefore signals a dynamical transition analogous to the (adiabatic) Gardner transition in the limit  $d \rightarrow \infty$ , where the landscape becomes truly rough. Unlike the adiabatic transition, however, this dynamical transition can be observed for *all*  $\hat{\varphi}_{\text{in}}$ .

Figure 5(b) reports the dimensional evolution of  $\hat{\varphi}_{dG} = \langle \hat{\varphi}_{\text{VV}} \rangle$ , which in the limit  $d \rightarrow \infty$  defines a dynamical Gardner transition. Unlike the jamming transition,  $\hat{\varphi}_{dG}$  clearly scales as  $1/d$ , consistent with compact rather than rough landscape features controlling its position. It is hence possible to robustly extrapolate

to the limit  $d \rightarrow \infty$ . Interestingly, near  $\hat{\varphi}_{\text{in}} \gtrsim \hat{\varphi}_d$  the adiabatic and the dynamical Gardner transitions are clearly distinct, with  $\hat{\varphi}_{dG} > \hat{\varphi}_G$ . For  $\hat{\varphi}_{\text{in}} \gg \hat{\varphi}_d$ , however, the two nearly coincide. In this regime, cages are well formed and fluctuations are small [32], and hence slow and fast compressions experience similar landscape roughness. For  $\hat{\varphi}_{\text{in}} < \hat{\varphi}_d$ , no adiabatic transition exists, but the dynamical one smoothly continues across. The density gap between the jamming and the dynamical Gardner transitions further grows as  $\hat{\varphi}_{\text{in}}$  decreases and persists even at  $\hat{\varphi}_{\text{in}} = 0$ . Finite- $d$  echoes of this physics should therefore be discernible along the compression trajectory of even the simplest of jamming systems, at least for  $d > 2$ .

*Jamming Universality* – Independent on the particular compression algorithm, isostatic jammed configurations have been reported to exhibit robustly universal properties. For many-body systems quantitative theoretical predictions obtained in the limit  $d \rightarrow \infty$  [11] have been indeed been found to persist down to  $d = 2$  [19–21]. Given that these critical scalings only emerge in the thermodynamic limit, this collective effect would not be expected to hold as-is for the single-particle RLG. The distribution of gaps between non-touching obstacles, for instance, remains far from the  $d \rightarrow \infty$  scaling with  $\gamma = 0.4127\dots$  at the higher  $d$  reached (see Fig. 6(a):inset). The small force distribution, however, does exhibit a clean power-law regime with the predicted exponent,  $\theta = 0.4231\dots$ , even in fairly low  $d$ , as verified by the finite-size scaling analysis of Fig. 6(a) (for VA-max results; other algorithms not shown); see details in App. G. The difference between the two observables is consistent with their finite-size dependence in many-body systems [21]. While the anomalous force distribution can be observed even in fairly small systems, hints of the gap one require systems with at least 200 particles to emerge.

More striking is that the geometry of isostatic contact vectors is robust even for small  $d$ . Different algorithms achieve IS with similarly distributed obstacles. As shown in Fig. 6(b), for instance, the cumulative distribution of the  $k$ -smallest force,  $f_k$ , for  $k = 1 \dots 4$  changes with dimensions but not with algorithm. VA-max, CALiPPSO, VA-min, and even a uniform sampling over IS give nearly indistinguishable results down to  $d = 4$ . In other words, the structural universality of jamming is present already in small  $d$ , encoded by the landscape and independent of dynamics. The algorithm merely sets the overall scale. A purely geometric analysis should therefore be able to extract this quantity and hence fully explain the jamming universality.

*Conclusions* – In this work, we have studied the landscape geometry and the volume ascent (VA) class of optimization algorithms for a paradigmatic model of real-space jamming, the random Lorentz gas (RLG). By analytically studying the complexity of its inherent

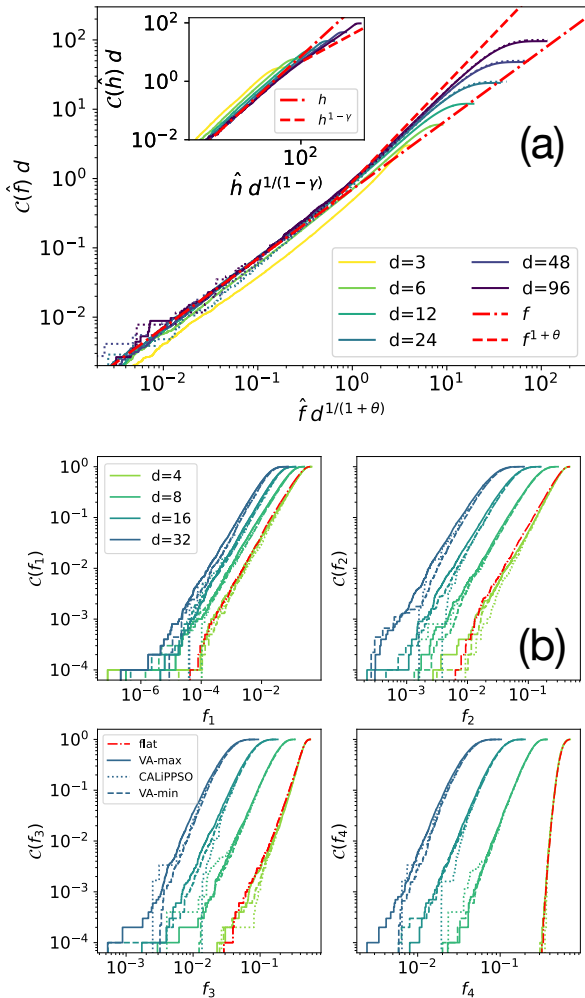


FIG. 6. **(a):** (Scaled) Cumulative force distribution for VA-max IS reached from  $\varphi_{\text{in}} = 0$ . Simulations from dimension  $d = 2$  to  $d = 96$  for systems of  $M = 1000d^2$  obstacles ( $M = 4 \times 10^6$  for  $d = 96$ ), with rescaled force  $\hat{f} = f/\langle f \rangle$ . The dashed line shows the  $d \rightarrow \infty$  power-law scaling prediction,  $f^{1+\theta}$  with  $\theta = 0.4231 \dots$ . Finite- $d$  corrections are included, thus resulting in a very good collapse and a clear crossover from the anomalous power-law to the linear regime (dash-dotted). (inset) The cumulative gap distribution does not similarly present an anomalous regime (with  $\gamma = 0.4127 \dots$ ), consistent with expectation of larger finite- $d$  corrections (see text). **(b):** Cumulative distribution of the smallest  $f_k$  contact force for  $k = 1 \dots 4$  for each IS in  $d = 4, 8, 16, 32$ . For each force type and each dimension, four different algorithms are considered: VA-max, CALiPPSO, VA-min, and uniform sampling. Despite strong algorithmic difference in IS sampling, the force distributions appear unchanged, thus supporting the universality of jamming physics.

structures (IS), we have shown that in large dimensions, (phase) space is almost completely filled with volumes that are unstable under compression and identified the geometric origin of the ensuing landscape roughness. The basins of attraction therefore exhibit a growing

hierarchical and fractal structure as  $d$  increases. The greedy VA-max algorithm was further argued to be an optimal choice for computing  $\varphi_{J0}$ .

Through the landscape analysis, we have identified en passant, a dynamical analogue of a Gardner transition that should be experimentally accessible and shown that static analytical predictions for  $d \rightarrow \infty$  agree with this definition for VA-max. We have also found that the structure of jammed configurations is independent of the jamming algorithm and matches mean-field predictions, thus identifying the geometric origin of jamming universality.

Several research directions in jamming physics stem from the current work. First, a generalization of VA-max to multi-particle systems should be possible. Given the lower computational complexity of the algorithm compared to previous proposals, a thermodynamic estimate of  $\varphi_{J0}$  – a more physically robust quantity than random close packing – should be within reach. Second, the graph structure of the landscape roughness within the “dynamical” Gardner phase and its fractal geometry could be directly compared with fullRSB calculation results. Third, the solution of the dynamical mean-field equations related to the VA-max algorithm is expected not to present the integration difficulties previously encountered in other out-of-equilibrium dynamics. An exact solution of the scheme in the limit  $d \rightarrow \infty$  should therefore be within reach. Fourth, the algorithmic robustness of jamming could be used to derive scaling laws from a purely geometrical approach.

In addition, the present work sheds new light on the broader class of real-space optimization problems in complex landscapes. “Computing largest empty circles with location constraints” [58] is a fundamental problem in robust optimization [36, 59, 60]. Although heuristic algorithms can approximate the optimal solution in any dimension [61], the best optimizers are based on the Voronoi tessellation [58, 62, 63], which is computationally prohibitive in high dimensions, as it requires  $O(n^{\lceil d/2 \rceil})$  operations for  $n$  constraints. The VA-edge class provides a geometrically intuitive and computationally efficient approach to this problem. By analogy to simulated annealing, the reluctant VA-min algorithm can find robust optimal configurations for a modest computational cost,  $O(nd^3)$ .

*Acknowledgments*– GF thanks Gilles Bonnet for a fruitful insight. This work was supported by a grant from the Simons Foundation (Grant No. 454937 to PC) and by ICSC - Italian Research Center on High-Performance Computing, Big Data, and Quantum Computing, funded by the European Union - NextGenerationEU. GF further acknowledges support from a postdoctoral fellowship from the Duke Center on Computational Thinking. Data relevant to this work have been archived and can be accessed at the Duke Digital Repository <https://doi.org/10.7924/XXXXXX>.

- 
- \* giampaolofolena@gmail.com
- [1] D. Frenkel, The tetrahedral dice are cast ... and pack densely, *Physics* **3**, 3 (2010).
  - [2] A. J. Liu and S. R. Nagel, Jamming is not just cool any more, *Nature* **396**, 21 (1998).
  - [3] M. Manti, V. Cacucciolo, and M. Cianchetti, Stiffening in soft robotics: A review of the state of the art, *IEEE Robotics Autom. Mag.* **23**, 93 (2016).
  - [4] E. Lawson-Keister and M. L. Manning, Jamming and arrest of cell motion in biological tissues, *Curr. Opin. Cell Biol.* **72**, 146 (2021).
  - [5] S. Spigler, M. Geiger, S. d'Ascoli, L. Sagun, G. Biroli, and M. Wyart, A jamming transition from under- to over-parametrization affects generalization in deep learning, *J. Phys. A* **52**, 474001 (2019).
  - [6] S. d'Ascoli, M. Refinetti, G. Biroli, and F. Krzakala, Double trouble in double descent: Bias and variance (s) in the lazy regime, in *International Conference on Machine Learning* (PMLR, 2020) pp. 2280–2290.
  - [7] A. J. Liu and S. R. Nagel, The jamming transition and the marginally jammed solid, *Annu. Rev. Condens. Matter Phys.* **1**, 347 (2010).
  - [8] L. Berthier and G. Biroli, Theoretical perspective on the glass transition and amorphous materials, *Rev. Mod. Phys.* **83**, 587 (2011).
  - [9] S. Torquato and F. H. Stillinger, Jammed hard-particle packings: From Kepler to Bernal and beyond, *Rev. Mod. Phys.* **82**, 2633 (2010).
  - [10] P. Charbonneau, J. Kurchan, G. Parisi, P. Urbani, and F. Zamponi, Glass and jamming transitions: From exact results to finite-dimensional descriptions, *Annu. Rev. Condens. Matter Phys.* **8**, 265 (2017).
  - [11] G. Parisi, P. Urbani, and F. Zamponi, *Theory of Simple Glasses: Exact Solutions in Infinite Dimensions* (Cambridge University Press, 2020).
  - [12] P. Charbonneau, J. Kurchan, G. Parisi, P. Urbani, and F. Zamponi, Fractal free energy landscapes in structural glasses, *Nat. Commun.* **5**, 3725 (2014).
  - [13] P. Charbonneau, J. Kurchan, G. Parisi, P. Urbani, and F. Zamponi, Exact theory of dense amorphous hard spheres in high dimension. III. The full replica symmetry breaking solution, *J. Stat. Mech.* **2014**, P10009 (2014).
  - [14] M. Wyart, Marginal stability constrains force and pair distributions at random close packing, *Phys. Rev. Lett.* **109**, 125502 (2012).
  - [15] E. Lerner, G. Düring, and M. Wyart, Low-energy nonlinear excitations in sphere packings, *Soft Matter* **9**, 8252 (2013).
  - [16] M. Müller and M. Wyart, Marginal stability in structural, spin, and electron glasses, *Annu. Rev. Condens. Matter Phys.* **6**, 177 (2015).
  - [17] A. Donev, S. Torquato, and F. H. Stillinger, Pair correlation function characteristics of nearly jammed disordered and ordered hard-sphere packings, *Phys. Rev. E* **71**, 011105 (2005).
  - [18] M. Skoge, A. Donev, F. H. Stillinger, and S. Torquato, Packing hyperspheres in high-dimensional Euclidean spaces, *Phys. Rev. E* **74**, 041127 (2006).
  - [19] P. Charbonneau, E. I. Corwin, G. Parisi, and F. Zamponi, Universal microstructure and mechanical stability of jammed packings, *Phys. Rev. Lett.* **109**, 205501 (2012).
  - [20] P. Charbonneau, E. I. Corwin, G. Parisi, and F. Zamponi, Jamming criticality revealed by removing localized buckling excitations, *Phys. Rev. Lett.* **114**, 125504 (2015).
  - [21] P. Charbonneau, E. I. Corwin, R. C. Dennis, R. Díaz Hernández Rojas, H. Ikeda, G. Parisi, and F. Ricci-Tersenghi, Finite-size effects in the microscopic critical properties of jammed configurations: A comprehensive study of the effects of different types of disorder, *Phys. Rev. E* **104**, 014102 (2021).
  - [22] V. Babu and S. Sastry, Criticality and marginal stability of the shear jamming transition of frictionless soft spheres, *Phys. Rev. E* **105**, L042901 (2022).
  - [23] Y. Wang, J. Shang, Y. Jin, and J. Zhang, Experimental observations of marginal criticality in granular materials, *Proc. Natl. Acad. Sci. U.S.A.* **119**, e2204879119 (2022).
  - [24] S. Torquato, T. M. Truskett, and P. G. Debenedetti, Is random close packing of spheres well defined?, *Phys. Rev. Lett.* **84**, 2064 (2000).
  - [25] P. K. Morse and P. Charbonneau, Amorphous packings of spheres, in *Packing Problems in Soft Matter Physics*, edited by H.-K. Chan, S. Hutzler, A. Mughal, C. S. O'Hern, Y. Wang, and D. Weaire (Royal Society of Chemistry, Cambridge, 2025) p. in press.
  - [26] M. Ozawa, T. Kuroiwa, A. Ikeda, and K. Miyazaki, Jamming transition and inherent structures of hard spheres and disks, *Phys. Rev. Lett.* **109**, 205701 (2012).
  - [27] S. Chiu, D. Stoyan, W. Kendall, and J. Mecke, *Stochastic Geometry and Its Applications*, Wiley Series in Probability and Statistics (Wiley, 2013).
  - [28] F. H. Stillinger and T. A. Weber, Inherent structure theory of liquids in the hard-sphere limit, *J. Chem. Phys.* **83**, 4767 (1985).
  - [29] S. Torquato and Y. Jiao, Robust algorithm to generate a diverse class of dense disordered and ordered sphere packings via linear programming, *Phys. Rev. E* **82**, 061302 (2010).
  - [30] C. Artiago, R. Díaz Hernández Rojas, G. Parisi, and F. Ricci-Tersenghi, Hard-sphere jamming through the lens of linear optimization, *Phys. Rev. E* **106**, 055310 (2022).
  - [31] A. Manacorda and F. Zamponi, Gradient descent dynamics and the jamming transition in infinite dimensions, *J. Phys. A* **55**, 334001 (2022).
  - [32] G. Bonnet, P. Charbonneau, and G. Folena, Glasslike caging with random planes, *Phys. Rev. E* **109**, 024125 (2024).
  - [33] M. De Berg, *Computational geometry: algorithms and applications* (Springer Science & Business Media, 2000).
  - [34] F. P. Preparata and M. I. Shamos, *Computational geometry: an introduction* (Springer Science & Business Media, 2012).
  - [35] C. D. Toth, J. O'Rourke, and J. E. Goodman, *Handbook of discrete and computational geometry* (CRC press, 2017).
  - [36] A. Ben-Tal, L. El Ghaoui, and A. Nemirovski, *Robust optimization*, Vol. 28 (Princeton university press, 2009).
  - [37] P. K. Morse and E. I. Corwin, Local stability of spheres via the convex hull and the radical Voronoi diagram, *Phys. Rev. E* **108**, 064901 (2023).

- [38] Note that these numbers are known exactly up to  $d = 4$ [39]:  $N_{\text{DS}}(d = 2) = 2$ ,  $N_{\text{DS}}(3) = 6.76\dots$ ,  $N_{\text{DS}}(4) = 31.77\dots$
- [39] H. Edelsbrunner, A. Nikitenko, and M. Reitzner, Expected sizes of Poisson–Delaunay mosaics and their discrete Morse functions, *Adv. Appl. Probab.* **49**, 745 (2017).
- [40] R. Schneider and W. Weil, *Stochastic and Integral Geometry*, Probability and Its Applications (Springer Berlin Heidelberg, 2008).
- [41] We thank Gilles Bonnet for suggesting this invariance.
- [42] This ratio is akin to that obtained from Wendel’s theorem [64], which predicts that a proportion  $1/2^d$  of stable simplexes is obtained when sampling  $d+1$  vertices on a  $d$ -dimensional sphere. The two cases, however, differ because the random Delaunay simplexes considered here tend to be more stable than random simplexes.
- [43] F. H. Clarke, *Optimization and nonsmooth analysis* (SIAM, 1990).
- [44] M. Gaudioso, G. Giallombardo, and G. Miglionico, Essentials of numerical nonsmooth optimization, *4OR* **18**, 1 (2020).
- [45] This process is equivalent to projecting the initial point onto one of the vertexes of the Voronoi polytope defined by points that are closer to  $\mathbf{x}_1$  than to any other obstacle.
- [46] G. Parisi, On the statistical properties of the large time zero temperature dynamics of the SK model, *Fractals* **11**, 161 (2003).
- [47] S. F. Edwards and R. B. S. Oakeshott, Theory of powders, *Physica A* **157**, 1080 (1989).
- [48] A. Baule, F. Morone, H. J. Herrmann, and H. A. Makse, Edwards statistical mechanics for jammed granular matter, *Rev. Mod. Phys.* **90**, 015006 (2018).
- [49] G. Folena, S. Franz, and F. Ricci-Tersenghi, Rethinking mean-field glassy dynamics and its relation with the energy landscape: The surprising case of the spherical mixed  $p$ -spin model, *Phys. Rev. X* **10**, 031045 (2020).
- [50] G. Folena, S. Franz, and F. Ricci-Tersenghi, Gradient descent dynamics in the mixed  $p$ -spin spherical model: finite-size simulations and comparison with mean-field integration, *J. Stat. Mech.* **2021**, 033302 (2021).
- [51] G. Folena and F. Zamponi, On weak ergodicity breaking in mean-field spin glasses, *SciPost Phys.* **15**, 109 (2023).
- [52] E. Lerner, G. Düring, and M. Wyart, Simulations of driven overdamped frictionless hard spheres, *Comput. Phys. Commun.* **184**, 628 (2013).
- [53] P. Charbonneau and P. K. Morse, Memory formation in jammed hard spheres, *Phys. Rev. Lett.* **126**, 088001 (2021).
- [54] G. Biroli, P. Charbonneau, G. Folena, Y. Hu, and F. Zamponi, Local dynamical heterogeneity in simple glass formers, *Phys. Rev. Lett.* **128**, 175501 (2022).
- [55] P. Charbonneau, Y. Hu, and P. K. Morse, Dynamics and fluctuations of minimally structured glass formers, *Phys. Rev. E* **109**, 054905 (2024).
- [56] V. Erba, F. Behrens, F. Krzakala, and L. Zdeborová, Quenches in the Sherrington–Kirkpatrick model, *J. Stat. Mech.* **2024**, 083302 (2024).
- [57] P. Charbonneau and P. K. Morse, Jamming, relaxation, and memory in a minimally structured glass former, *Phys. Rev. E* **108**, 054102 (2023).
- [58] G. T. Toussaint, Computing largest empty circles with location constraints, *Int. J. Comput. Inf. Sci.* **12**, 347 (1983).
- [59] D. Bertsimas, O. Nohadani, and K. M. Teo, Robust optimization for unconstrained simulation-based problems, *Oper. Res.* **58**, 161 (2010).
- [60] D. Bertsimas, D. B. Brown, and C. Caramanis, Theory and applications of robust optimization, *SIAM Rev.* **53**, 464 (2011).
- [61] M. Hughes, M. Goerigk, and M. Wright, A largest empty hypersphere metaheuristic for robust optimisation with implementation uncertainty, *Comput. Oper. Res.* **103**, 64 (2019).
- [62] B. Chazelle, An optimal convex hull algorithm in any fixed dimension, *Discrete Comput. Geom.* **10**, 377 (1993).
- [63] A. Okabe and A. Suzuki, Locational optimization problems solved through Voronoi diagrams, *Eur. J. Oper. Res.* **98**, 445 (1997).
- [64] J. G. Wendel, A problem in geometric probability., *Math. Scand.* **11**, 109–112 (1962).
- [65] The computational complexity of the linear optimization algorithm arises not from evaluating the circumcenter, but from identifying which DS contains the point.
- [66] P. Rathie, On the volume distribution of the typical Poisson–Delaunay cell, *J. Appl. Probab.* **29**, 740 (1992).
- [67] C. B. Barber, D. P. Dobkin, and H. Huhdanpaa, The Quickhull algorithm for convex hulls, *ACM Trans. Math. Softw.* **22**, 469 (1996).

## Supplementary Material

### Appendix A: VA-edge algorithm

The VA-edge algorithm consists of three parts: (1) initializing the system by a sampling of  $M$  points (corresponding to obstacle centers) uniformly at random within a spherical shell around the origin; (2) initiating the dynamics from the origin in the direction radial to the closest center, thus defining a Voronoi polytope, and proceeding for  $d$  projection steps on the Voronoi faces, until reaching one vertex of the polytope; (3) evolving the dynamics on edges of the Voronoi tessellation until reaching a stable vertex (i.e. an IS). Details can be found in Algorithm 1.

---

#### Algorithm1 VA-edge algorithm

---

1. radially sample  $M$  points  $\{\mathbf{o}_i\}_{i=1}^M$  in  $d$  dimensions around the origin  $(0, \dots, 0)$ .
  2. project onto one edge of the initial Voronoi polytope
    - (a) select the closest center  $\mathbf{p}_0$ , which is the center of initial Voronoi polytope  
 $\mathbf{p}_0 = \operatorname{argmin}_{\mathbf{o}_i}(|\mathbf{o}_i|)$
    - (b) initiate the dynamics at the origin  $\mathbf{x}_{\text{in}} = \mathbf{x}_0 = (0, \dots, 0)$  with an initial unitary velocity radial from  $\mathbf{p}_0$   
 $\hat{\mathbf{v}}_0 = -\frac{\mathbf{p}_0}{|\mathbf{p}_0|}$
    - (c) proceed by projecting  $\mathbf{v}_0$  on hyperplanes defined by successive closest points  $\mathbf{p}_j$ ,
 

```

for  $j = 1; j < d + 1; j ++$  do
  for  $i = 0; i < M; i ++$  do
    if  $\mathbf{o}_i \notin \{\mathbf{p}_k\}_{k=0}^{j-1}$  then
       $l_i = \frac{|\mathbf{o}_i| - \mathbf{x}_{j-1} \cdot \mathbf{o}_i}{\hat{\mathbf{v}}_{j-1} \cdot \mathbf{o}_i}$ 
      ▷ if point does not already define VV
      ▷ distance of  $\mathbf{x}_{j-1}$  in  $\hat{\mathbf{v}}_{j-1}$  direction from new  $\mathbf{o}_i$ 
    end if
  end for
   $\mathbf{p}_j = \operatorname{argmin}_{\mathbf{o}_i}(l_i)$ 
  ▷ closest point in  $\hat{\mathbf{v}}_{j-1}$  direction
   $\mathbf{x}_j = \mathbf{x}_{j-1} + l_j \hat{\mathbf{v}}_{j-1}$ 
  ▷ update the position
   $\mathbf{v}_j = \hat{\mathbf{v}}_{j-1} - \mathbf{P}_{\{\mathbf{p}_k\}_{k=0}^j} \hat{\mathbf{v}}_{j-1}$ 
  ▷ project velocity into space  $\perp$  to space spanned by  $\{\mathbf{p}_k\}_{k=0}^j$ 
   $\hat{\mathbf{v}}_j = \operatorname{sign}(\mathbf{v}_j \cdot \mathbf{x}_{j-1}) \frac{\mathbf{v}_j}{|\mathbf{v}_j|}$ 
  ▷ define the expanding orientation and renormalize the velocity
end for

```
  3. VA walk on Voronoi vertices until a stable one is identified
 

```

while  $\mathcal{C}(\{\mathbf{p}_k\}_{k=0}^d) \notin \mathcal{S}(\{\mathbf{p}_k\}_{k=0}^d)$  do
  ▷ check if stable, i.e. if  $\mathcal{C}$  is contained in corresponding simplex  $\mathcal{S}$ 
   $\mathbf{x} = \mathcal{C}(\{\mathbf{p}_k\}_{k=0}^d), r = \mathcal{R}(\{\mathbf{p}_k\}_{k=0}^d)$ 
  ▷ define actual VV and respective radius (aka  $r_{\text{SPH}}$ )
  for  $j = 0; j < d; j ++$  do
    ▷ find expansion directions
     $\mathbf{c}_j = \mathcal{C}(\{\mathbf{p}_k\}_{k \neq j}^d), r_j = \mathcal{R}(\{\mathbf{p}_k\}_{k \neq j}^d)$ 
    ▷ define circumcenter and radius of  $(d-1)$ -simplex when excluding point
  end for
   $\mathbf{p}_j$ 
   $\mathbf{e}_j = \mathbf{x} - \mathbf{c}_j$ 
  ▷ define Voronoi edge vector when excluding point  $\mathbf{p}_j$ 
  if  $\mathbf{e}_j \cdot (\mathbf{p}_j - \mathbf{x}) < \mathbf{e}_* \cdot (\mathbf{p}_* - \mathbf{x})$  then
    ▷ growth on edge  $j$  from  $\mathbf{p}_j$  must be smaller than for some  $* \neq j$ 
    append  $j$  to  $J$ 
    ▷  $J$  is the list of expanding edges
  end if
end for
   $k_{\text{max}} = \operatorname{argmax}_{k \in J}(\frac{|\mathbf{e}_j|}{r_j})$ 
  ▷ define direction of maximal expansion for VA-max (alternatively, argmin for VA-min)
   $\hat{\mathbf{v}} = \frac{\mathbf{e}_{k_{\text{max}}}}{|\mathbf{e}_{k_{\text{max}}}|}, \hat{r} = r_{k_{\text{max}}}$ 
  ▷ unit vector along edge of maximal expansion and respective radius
  for  $i = 0; i < M; i ++$  do
    if  $\mathbf{o}_i \notin \{\mathbf{p}_k\}_{k=0}^d$  then
      ▷ if point does not already define VV
       $\alpha_i = \frac{|\mathbf{o}_i - \mathbf{x}|^2 - \hat{r}^2}{2\hat{\mathbf{v}} \cdot (\mathbf{o}_i - \mathbf{p}_{k_{\text{max}}})}$ 
      ▷  $\alpha_i$  is such that  $\mathbf{x} + \alpha_i \hat{\mathbf{v}}$  is equidistant from  $\{\mathbf{p}_k\}_{k \neq k_{\text{max}}}^d$  and  $\mathbf{o}_i$ 
    end if
  end for
   $i_{\text{new}} = \operatorname{argmin}_i(\alpha_i > 0)$ 
  ▷ select first point met expanding along the edge  $\hat{\mathbf{v}}$ 
   $\mathbf{p}_{k_{\text{max}}} = \mathbf{o}_{i_{\text{new}}}$ 
  ▷ substitute new point thus defining the new VV
end while

```
-

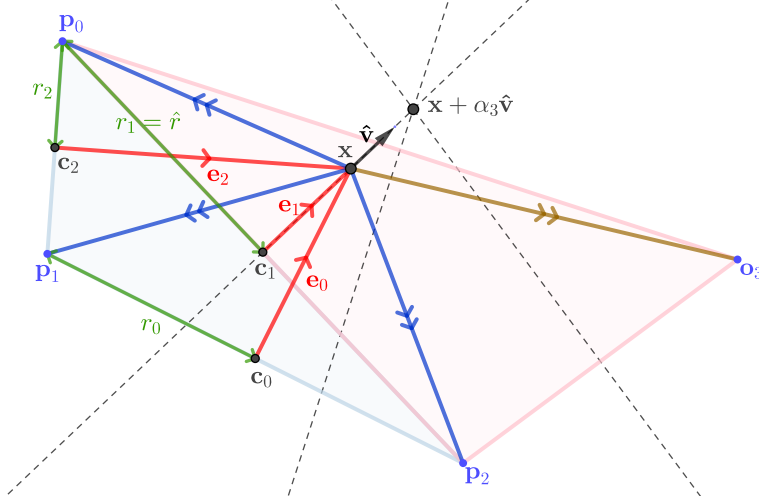


FIG. 7. Geometry in  $d = 2$  of one VA-max step between VVs as reported in part (3) of Algorithm 1.

### Appendix B: VA-edge computational efficiency

This appendix presents the dimensional scaling of several observables from VA-max and VA-min for various  $\hat{\varphi}_{\text{in}}$ . First, consider the total number of steps and the total displacement of the center of SPH, i.e. the length of the trajectory. As can be seen in Fig. 8, both quantities asymptotically increase with dimension and decrease with  $\hat{\varphi}_{\text{in}}$ . Moreover, the computational complexity of VA-max,  $O(d^2)$ , is always smaller than that of VA-min,  $O(d^3)$ . The low-polynomial scaling of VA-edge algorithms is non trivial. The number of unstable DS (or VVs) grows exponentially with  $d$ , and therefore a random walk on edges would take an exponential number of steps to reach an IS, as in typical NP-hard problems. The VA constraint of increasing  $r_{\text{SPH}}$ , however, poses a strong ordering to the exploration, thus making VA-edge algorithms run in polynomial time in the dimension of the explored space.

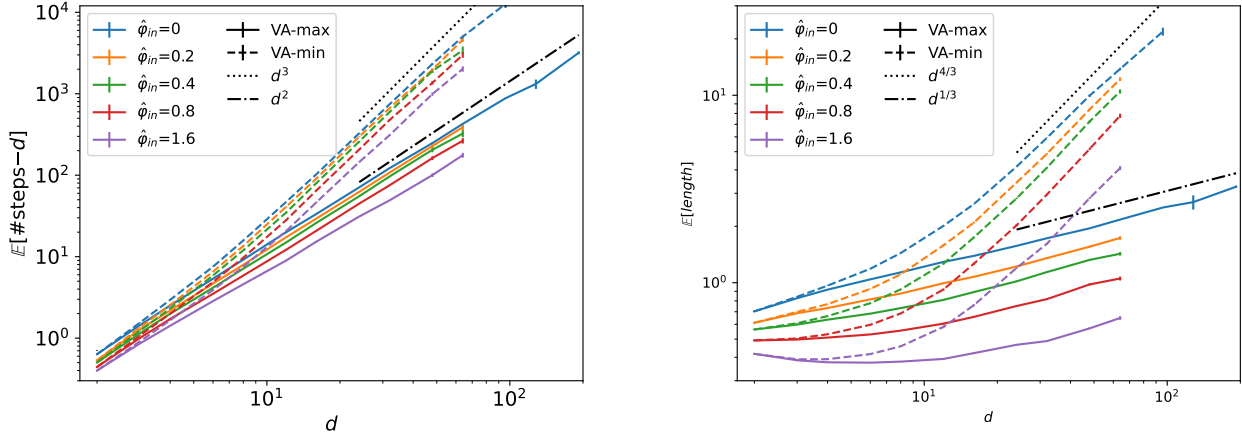


FIG. 8. (left): Dimensional evolution of the average number of steps (after the  $d$  steps of the initial projection) to reach an IS for  $\hat{\varphi}_{\text{in}} = 0, 0.2, 0.4, 0.8, 1.6$ . VA-max (full-line) reaches an IS in  $O(d^2)$  and VA-min (dashed-line) does so in  $O(d^3)$  steps. (right): Average length of the total trajectory of the center of the SPH to reach the IS. This quantity is also the total time if the center of the SPH evolves at a constant velocity.

The computational problem of finding an IS of large  $\hat{\varphi}$  is a common optimization problem, very similar in spirit to optimization problems that involve minimizing a cost or energy function. Our problem is defined in a high-dimensional space when  $d \gg 1$ , and the structure of solutions (i.e. IS) is strongly non-convex: this is the typical situation where algorithms can easily get trapped in suboptimal solutions and the optimal solution is hard to achieve (and sometimes even to approximate).

We have observed in Fig. 5(a) that different algorithms reach IS with different  $\hat{\varphi}$ . More importantly, we observe that for any  $d$  value VA-max and CALiPPSO reach the same value  $\hat{\varphi}_{\min}$ , while VA-min and force-min reach the same value  $\hat{\varphi}_{\max}$ . Two different algorithms reaching the same IS for any  $d$  value is hardly a coincidence and suggests  $\hat{\varphi}_{\min}$  and  $\hat{\varphi}_{\max}$  play an important role. Could they be threshold values for different classes of algorithms?

To try to answer to the above question, we recap what is known about the paradigmatic model for complex systems, the Sherrington–Kirkpatrick (SK) model. The model is composed of  $N$  Ising spins interacting through randomly chosen couplings (e.g. Gaussian couplings of zero mean and variance equal to  $1/N$ ). In the large  $N$  limit, the ground state energy is known from the Parisi solution, but it is not easy to attain by a polynomial-time algorithm. For example, it is well-known that greedy algorithms (i.e. algorithms decreasing the energy at each step, like the VA algorithms) reach different asymptotic energies depending on the degree of greediness: the most greedy version gets trapped far away from the ground state, while the most reluctant version approach closer the ground state [46]. Recently, Montanari presented an algorithm that approximates the ground state energy of the SK model to arbitrary precision in a time that scales quadratically with the system size (and inversely in the precision). Even more recently, the most reluctant algorithm has been reanalyzed [56] finding evidence it can approach the ground state energy in a time  $O(N^2)$  (while the most greedy version runs in a time  $O(N)$ ). The overall picture that comes out from the study of algorithms optimizing the SK model is that different energy thresholds exist for algorithms running in times scaling differently with the system size, that is, with the dimension of the space over which the function to be optimized is defined.

Our results on the computational complexity of the algorithms belonging to the VA-edge class perfectly fit into the above scenario. We have shown that the VA-max algorithm runs in a time  $O(d^2)$  and reaches a lower value  $\hat{\varphi}_{\min}$ . Instead, the VA-min algorithm runs in a time  $O(d^3)$  and reaches a much larger value  $\hat{\varphi}_{\max}$ . Given the above observations on the universality of these two threshold values, we are tempted to conjecture they correspond to algorithmic thresholds for classes of VA algorithms running on different time scales. Moreover, given that the difference between these two thresholds gets larger increasing  $d$ , the two algorithmic thresholds are clearly well separated in the large  $d$  limit.

The linear optimization algorithm CALiPPSO converges in a number of steps  $O(d)$ . Notice, however, that each step is non-local and costs at least  $O(d^2)$ . The overall complexity therefore scales as  $O(d^3)$ . Given that CALiPPSO and VA-max algorithms reach the same densities and the latter takes a time  $O(d^2)$ , we conclude the class of VA-edge algorithms is highly efficient compared to other optimization algorithms.

During the VA-edge dynamics at each vertex the algorithm has  $k$  different possible edges on which to expand. This number can be averaged during the whole trajectory for each trajectory. The proportion of expanding edges (i.e.  $k/d$ ) is shown in Fig. 9 to asymptotically increase with dimension and decrease with  $\hat{\varphi}_{\text{in}}$ . Note that the VA-max algorithm always sees more expanding direction, a signature of the fragility of trajectory and the final IS relative to those of VA-min. A similar result is expected for other reluctant VA-edge algorithms.

The difference between the final displacement of the SPH center  $|\mathbf{x}_{\text{IS}}|$  and the radius of SPH  $r_{\text{IS}}$  is shown in Fig. 9. This quantity is identically zero if the final IS has a radius that is in contact with the first encountered obstacle. For asymptotically large  $d$  this difference goes to zero for any  $\hat{\varphi}_{\text{in}}$ . In other words, in the limit  $d \rightarrow \infty$  the dynamics is confined to the Voronoi polytope in which it started. Studying the distribution properties of Poisson–Voronoi tessellations for large  $d$  should therefore suffice to understand the fate of the VA-edge dynamics and perhaps an analytical understanding of  $\hat{\varphi}_{\text{J0}}$  in the RLG through stochastic geometry would be possible.

### Appendix C: CALLiPSO and the RLG

The definition of Delaunay basin in Eq. (4) can be recast in a computationally powerful – albeit non-local VA – algorithm. In this scheme, the initial tracer position is first mapped to the circumcenter of the DS to which it belongs. That DS is either stable (i.e. an IS) or not. In the unstable case, the procedure is iterated until a stable DS is reached [65]. Each step is a *linear optimization* (LO) problem, and the resulting algorithm in jamming of multi-particle systems has been called CALiPPSO (for chain of approximate linear programming for packing spherical objects) [30].

VA-max and CALiPPSO are significantly different algorithms (see App. H). (i) VA-max follows an initial projection dynamics that has no equivalent in CALiPPSO. (ii) Both VA-max and CALiPPSO follow a VV-based dynamics, but VA-max follows the VA-edge that locally maximizes tracer growth, while CALiPPSO chooses the nearby VV that maximizes the growth of the tracer, hence directly optimizing the end point of each step. Both algorithms nevertheless follow a greedy path over VVs. In  $d = 2$ , if we exclude the initial projection of the VA-edge, the two schemes are equivalent in the RLG. But even in higher  $d$  their respective distributions of basins of

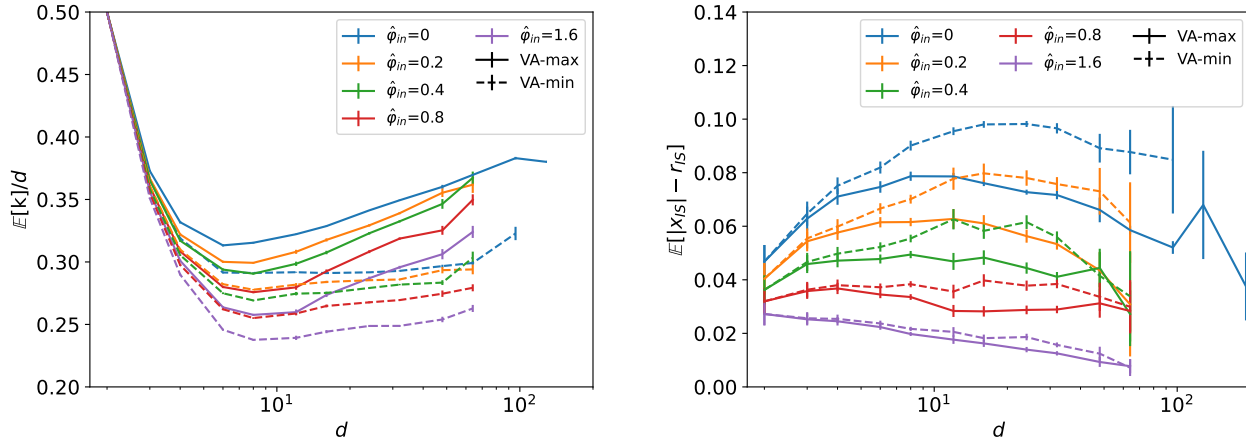


FIG. 9. (left): Average proportion of expanding directions over the VA trajectory as a function of  $d$  for different  $\hat{\phi}_{in}$ . VA-max (full-line) experiences more possible expanding directions than VA-min (dashed-line). (right): Average difference between the final displacement of the SPH center  $|\mathbf{x}_{IS}|$  and the radius of SPH  $r_{IS}$ . That difference is zero if the final IS has a  $r_{IS}$  that touches the closest initial obstacle to the tracer. The behavior for different  $\hat{\phi}_{in}$  suggests an asymptotic limit in which the  $r_{IS}$  always touches the first encountered obstacle.

attraction are fairly similar (see Fig. 5(a) inset). It is, however, unclear if the (near) correspondence holds also for multi-particle systems.

In the RLG scenario each step of the CALiPPSO algorithm consists of finding the circumcenter corresponding to the vertices of the Delaunay simplex that contains the tracer (i.e. finding the displacement of the tracer  $\mathbf{x}_{circ}$  that increases its radius  $r_{circ}$  the most), then updating the tracer position to this new center. Therefore, each step corresponds to  $\max_{\mathbf{x}_{circ}, r_{circ}} r_{circ}$  such that  $r_{circ} \leq |\mathbf{r}_i - \mathbf{x}_{circ}| \quad \forall i$ . This can be translated in the LO:

$$\begin{cases} \max_{\mathbf{x}_{circ}, \Gamma_{circ}} \Gamma_{circ} & \text{s.t.} \\ 2 \frac{\mathbf{r}_i}{|\mathbf{r}_i|} \cdot \mathbf{x}_{circ} + \frac{\Gamma_{circ}}{|\mathbf{r}_i|} \leq |\mathbf{r}_i| & \forall i \end{cases} \quad (\text{C1})$$

where  $\mathbf{r}_i$  is the position of the obstacle  $i$  with respect to the tracer,  $\mathbf{x}_{circ}$  is the position of the circumcenter of the Delaunay simplex containing the tracer and  $\Gamma_{circ}$  is a proxy for its radius  $r_{circ} = \sqrt{\Gamma_{circ} + |\mathbf{x}_{circ}|^2}$ . The computational complexity of each step is larger than  $O(d^2)$ . This algorithm is equivalent to that described in [30], and here simply reinterpreted for the RLG, in which case it becomes geometrically interpretable in terms of DS and corresponding circumcenters.

#### Appendix D: force-min and the RLG

One can also consider the force-min algorithm, which is an adaptation of the overdamped event driven algorithm first described in Ref. [52] wherein a hard particle system approaches jamming through athermal compression [57]. Adapting that algorithm to the RLG is conceptually and computationally straightforward; the result is part of the VA class. After the projection phase, the choice of direction within the VA cone is not based on the rate of volume increase along a VA-edge, but on the magnitude of the forces *applied* by the obstacles on the tracer. If a VV is unstable, then at least one of these forces is negative. The force-min algorithm prunes the contact with the largest negative force recursively until all forces are positive. If more than one force is removed, then an infinitesimal VA might cause the tracer to overlap with an obstacle. In that case, the removed contact that causes the largest overlap upon infinitesimal ascent is reconnected, and the algorithm returns to pruning forces. This procedure is followed until an IS is identified.

If no more than one VV is removed, the scheme is part of the VA-edge class. Otherwise, the trajectory goes through a Voronoi facet of larger dimension and is hence not part of that class. The final packing fraction nevertheless falls near the VA-min results (see Fig. 5(a)). A schematic recapitulating the various algorithms considered in this work is provided in Fig. 11.

## Appendix E: Mathematical Results

The Poisson–Voronoi/Delaunay tessellation offers a minimal model of random tessellations and has hence been intensively studied by mathematicians and computer scientists. For example, the volume distribution of Poisson–Delaunay simplexes [66] (see Fig. 10) and the distribution of circumradii of Delaunay simplexes [39] are known exactly. These results have here been used to validate the RLG IS numerical simulations. However, to the best of our knowledge, no studies of polytopes formed by the union of one stable simplex and the surrounding unstable ones have previously been made. Therefore, in order to study the results of the compression algorithm, computer simulations remain the best option.

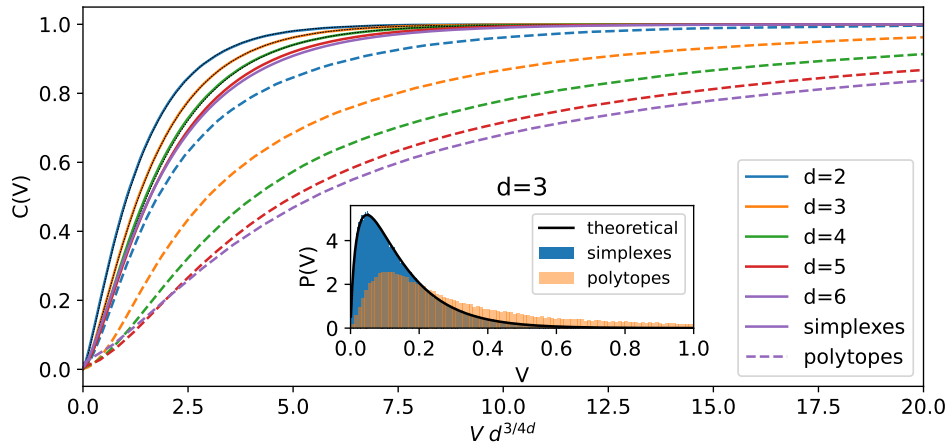


FIG. 10. Cumulative distribution of volume of simplexes (continuous) and polytopes (dashed) in the Poisson–Delaunay tessellation for  $d = 2, \dots, 6$ . The  $x$ -axis is rescaled for compactness. The polytopes identify the basins of IS for  $\varphi_{\text{in}} = 0$  obtained by agglomerating the stable simplex with the surrounding unstable ones. For simplexes the exact mathematical result is superimposed (thin dotted black line), but no comparable result exists for polytopes. The inset shows the respective probability distributions for  $d = 3$ .

## Appendix F: Numerical methods for the geometrical analysis

Each numerical simulation in this manuscript relies on sampling  $M$  Poisson-distributed points (obstacles) with  $\rho = 1$  inside a  $d$ -dimensional ball of radius  $R$ . This construction is achieved by radial sampling, following the approach in Ref. [32]. The choice of radius,  $R = (M/V_d)^{1/d}$ , is inherently related to the number of points  $M$  and the dimension  $d$ . In general,  $M$  is chosen based on the type of simulation being performed.

The geometrical properties of IS and corresponding Delaunay basins in the RLG – results shown in Fig. 2, Fig. 4 and the red dotted lines in Fig.2(b) – are evaluated numerically by exact Voronoi/Delaunay tessellation of 50 samples (using qhull [67] as in [32]). These samples contain  $M = 2000 \cdot d$  points for  $d = 2, \dots, 5$ , and  $M = 40,000$  points for  $d = 6$ . Due to the exponential scaling of numerical complexity with dimension, simulations are limited to  $d \leq 6$ . The results align well with the analytical predictions of the radius and volume distribution of simplexes, discussed in E (see Fig. 2 and Fig. 10).

For the compression analysis of different algorithms, the radius  $R$  is selected so that  $M = 1000d^2$  points are sampled. This scaling has been empirically found necessary to reach dimensions as high as  $d = 200$ . Given that the reduced packing fraction  $\hat{\varphi}$  is expected to converge to a finite value, and since  $d\hat{\varphi}IS$  represents the volume of a sphere with radius  $r_{IS}$ , and  $M$  equals the total volume of the simulation ball (since  $\rho = 1$ ), we expect to need at least  $M = O(d^1)$  for the simulation ball to contain the final SPH. However, accounting for the displacement of the center of the SPH, we have chosen  $M = O(d^2)$ .

## Appendix G: Finite-size analysis of the jamming critical distributions

The analysis we carried out is completely analogous to the one presented in [21] for the case of multi-particle jamming, so here we will only describe it briefly. The main idea is that if in the thermodynamic limit a random variable  $x$  follows a power-law pdf,  $p_X(x) \sim x^{-\alpha}$ , for a given  $\alpha$ , sampling  $x$  in finite systems will yield a distribution with a different exponent, say  $\alpha'$ . When  $p_X$  is related to criticality, then the main reason for having  $\alpha \neq \alpha'$  is not limited sampling but finite-size effects. That is, in finite systems with  $n$  degrees of freedom, there is a natural bound to any correlation length in the system, which cannot be larger than the system itself, i.e.  $\xi \sim L \sim n^{1/d}$ , so divergences in  $\xi$  are inevitably suppressed. This property, which initially seems a strong limitation, can actually be exploited to derive a rescaled variable  $\tilde{x}$ , which accounts for the effect of  $n$  and  $\alpha$  in the sampling of  $x$ , and the corresponding scaling function,  $\tilde{p}_X(\tilde{x})$ , which becomes independent of system size. Importantly, this is only the case when the correct value of  $\alpha$  is used for defining  $\tilde{x}$ . In practical terms, only if we accurately estimate  $\alpha$  do the empirical distributions of  $p_X$  – obtained from datasets of systems with different sizes – collapse into a single master curve, i.e., the scaling function.

Let us now consider the case of contact forces in the RLG, so  $x = f$  and we know the  $d \rightarrow \infty$  prediction is  $p_F(f) \sim f^{-\theta}$ , with  $\theta = 0.4231\dots$ . As explained in Ref. [21], to derive the scaling function of interest we need to consider that the smallest force in a sample,  $f_{min}$  typically behaves as  $\int_0^{f_{min}} p_F(f)df \sim f_{min}^{1+\theta} \sim 1/n$ . The next step is realizing that, while in multi-particle systems  $n = dN$ , in the RLG we have instead  $n = d + 1$ . In other words, the correct variable for which to consider finite-size effects is dimensionality itself. With this mapping in mind, we can directly use the equations from Ref. [21] and obtain the scaling variable for the forces,  $\tilde{f} = f d^{1/(1+\theta)}$  and  $\tilde{p}_F(\tilde{f}) \sim d^{\frac{\theta}{1+\theta}} p_F(f)$ . Additionally, size corrections to isostaticity are important because they cause the scaled pdf to behave as  $\tilde{p}_F(\tilde{f}) \sim 1$  for  $\tilde{f} \ll 1$ . To better compare with numerical data in the main text we considered the cumulative distributions,  $c(f) = \int_0^f p_F(f')df'$ , for which the corresponding scaling function reads

$$\tilde{c}(\tilde{f}) \sim dc(f) \sim \begin{cases} \tilde{f}^{1+\theta}, & \tilde{f} \gg 1 \\ \tilde{f}, & \tilde{f} \ll 1. \end{cases} \quad (\text{G1})$$

The first power-law scaling comes from the usual scaling regime where finite-size effects are incorporated into the thermodynamic-limit criticality, and therefore the dependence on  $\theta$ , while the linear behavior stems from finite  $d$  corrections to isostaticity. Given that the results in Fig. 6(a) accurately follow both regimes of Eq. (G1), provides solid evidence that jamming universality is present in the RLG.

## Appendix H: Scheme for algorithms used in this work

In Fig. 11 we present a summary scheme of the different classes of greedy algorithms for the RLG explored in this manuscript. On the left in the class of geometry-driven algorithms, the linear-optimization (LO) subclass approximates (at each step) the local geometry of growth with a convex polytope and update the position by linear optimization. In the RLG, the greediest (*known*) algorithm for this class is the CALiPPSO algorithm [30]. On the right the class of event-driven local (VA) algorithm of which the VA-edge is a subclass which follows Voronoi edges to search for growing directions. In the RLG, the greediest algorithm (*by construction*) for this class is the VA-max algorithm, which is analogous to a gradient descent algorithm for energy landscapes. VA-max and CALiPPSO are found to be asymptotically equivalent in large  $d$ . However, it is not clear if this equivalence remains true in finite dimensional systems. The force-min algorithm developed in [15] it reaches denser packings than the VA-max and is therefore a sub-greedy (more reluctant) version.

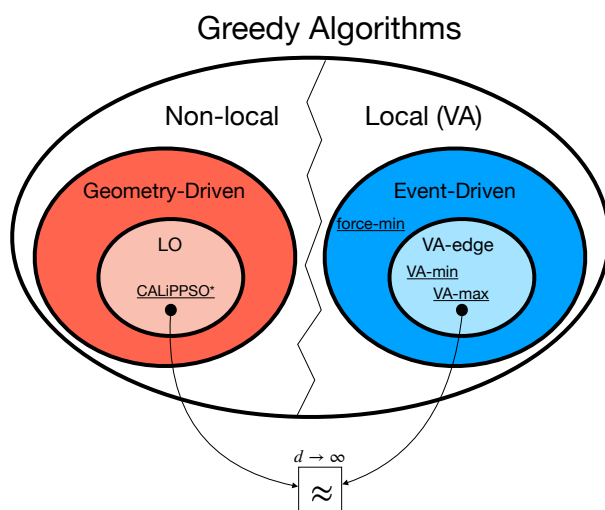


FIG. 11. Scheme of the different classes of greedy algorithms for the RLG explored in this manuscript.